2023 IEEE International Conference on Robotics and Automation (ICRA 2023)
May 29 - June 2, 2023. London, UK

On Tendon Driven Continuum Robots with Compressible Backbones

Manu Srivastava
Electrical and Computer Engineering
Clemson University, USA
manus@clemson.edu

Ian D. Walker
Electrical and Computer Engineering
Clemson University, USA
iwalker@clemson.edu

***Abstract*—This paper discusses the effect of axial backbone compression on tendon-driven continuum robots. A new mechanics model for compensating for this effect that does not require tendon tension sensing or knowledge of manipulator material properties/stiffnesses is introduced and analyzed. In addition, we provide an analytical expression for the minimum preload on the tendons to achieve a given bend, a quantity determined empirically thus far. Our model is computationally efficient and achieves real time control on low cost hardware. The analysis is supported by experimental results demonstrating significant improvement over kinematics in open loop control of a tendon-driven continuum hose robot.**

***Index Terms*—continuum, mechanics, control**

I. Introduction

Continuous backbone "continuum" robots [1], [2] have become increasingly prominent within the robotics research community. They have been successfully applied to a wide variety of procedures in medicine [3]. Other demonstrated applications of continuum robots include inspection and repair of aero engines [4] and nuclear reactors [5] and 3D printing of cement [6]. Further applications, e.g. in agriculture [7], Space [8], and home healthcare (aging in place) [9] have been proposed and are being actively investigated.

A significant portion of existing continuum robot designs feature remote actuation using tendons [10], [11], [12], [13] [14]. Tendons are an attractive design choice because they offer relatively high actuation forces in a low profile design. However, implementation of tendon-actuated systems in general, and Tendon-Driven Continuum Robots (TDCRs) in particular, also presents challenges, arising from the unidirectional nature of tendons (they can pull but not push) and the challenges inherent in maintaining tension in them.

A key motivation for the use of continuum robots is exploitation of their compliance in bending (for example in adaptive whole arm grasping and navigation/inspection of congested environments [15]). However, compliance elsewhere in their structures, if not compensated for, can significantly reduce their effectiveness. Tendon-induced backbone compression and/or tendon extension caused by tendon actuation forces is present in almost all tendon driven continuum robot hardware. Kinematics for TDCRs [16], [17] can not account for either effect since modeling forces is outside the domain of kinematics. Therefore, widely used inverse kinematics based control of TDCRs for spatial bending can result in undesirable unmodeled effects, e.g. non-uniform curvature and end effector (EE) speed in different bend planes.

Models reflecting the mechanics and dynamics of TDCRs have been established [18], [19], [20], [21], [22]. However, consideration of axial compression in backbones remains rare. The results in [23], [24] and [25] developed models that described the effects of both axial backbone compression and tendon elasticity. However, the approach in [23] focuses on bending under external loading with knowledge of material properties, and that in [24] and [25], which as in this work address the issue of control, required both tendon tension sensing and identification of robot materials properties, as well as the need to filter input configurations for feasibility. Tendon tension sensing is present in some TDCR systems [26], [27] but is relatively uncommon and adds significant complexity.

In this paper, we introduce a new approach to modeling and handling compliance due to axial compression. The approach uses simple beam bending theory and exploits geometric symmetry in the design of TDCRs. In contrast to previously proposed methods, our approach does not require either the estimation of robot materials properties or tendon tension sensing. It also avoids the need for filtering of input configurations while guaranteeing that the tendons never become slack. We will refer to this model as the EC (Elasticity Compensation) model. Experimental results with a tendon-driven hose robot, which features significant axial compression, demonstrate the effectiveness of the approach.

II. Methods

We look at beam bending under the assumptions made in [24], listed below -

1) superposition of strain
2) linear elasticity in both axial compression and pure beam bending
3) plain strain
4) Saint Venant's principle for internal load distribution
5) cross-sections remain planar under bending

*This work was supported by U.S. National Science Foundation grants 1924721 and 2221126. The content is solely the responsibility of the authors and does not necessarily represent the official views of the NSF.

6) isotropic material properties

A. Setup

Our approach works for n-tendons but we will motivate it by using three tendons - the minimum number of tendons required for spatial bending.

Consider a continuum section of initial length, s, actuated by three symmetrically located tendons, bending in the ϕ plane with longitudinally variable centroidal axis curvature, κ_{ca}. From bending theory, the neutral axis, na, of a beam undergoing bending deformation is a longitudinal axis that experiences zero tension and as a result does not extend or compress during bending. Its length therefore remains unchanged at the original section length s. A longitudinal neutral surface, ns, is defined as a set of such axes. Since planar cross sections remain planar after deformation, the ns intersects any cross section in a straight line orthogonal to the bending plane. Subsequent references to na will refer to that na which is located in the bending or ϕ plane and intersects any cross section at a point.

Now consider a longitudinal differential element of the section with constant pre-bending initial thickness, ds, located at s. Post bending it is still located at s along the na with local curvatures $\kappa_{na}(s)$ and $\kappa_{ca}(s)$ of the na and ca respectively, as shown in Fig. 1. We now define the uniform strain over the cross-section due to axial compression, $\epsilon_a(s)$, as a function of s to account for possible variable curvature of the section's backbone:

$$\epsilon_a(s) = \frac{ds - ds'}{ds} \tag{1}$$

where ds' is the thickness of the ca contained within the differential element after compression, shown later in (5).

The na and ca curvatures are related by,

$$\kappa_{na}(s) = (1 - \epsilon_{ca}(s))\kappa_{ca}(s) \tag{2}$$

For simplicity of notation, we suppress the dependence on element location, s.

The assumption of superposition of strain, allows us to consider the pure bending strains due to multiple tendons and the strain due to axial compression separately. Pure bending implies that the na lies at the center of the beam. The linear strain due to pure bending, $\epsilon_b(x)$, is given by:

$$\epsilon_b(x) = \kappa_{na} x \tag{3}$$

where x is measured from the center in the ϕ plane.

The linear strain in the ϕ plane, $\epsilon(x)$ is therefore given by:

$$\epsilon(x) = \epsilon_a + \epsilon_b(x) \tag{4}$$

At the backbone or the ca, $x = 0$, and (3) and (4) imply:

$$\epsilon(0) = \epsilon_a = \epsilon_{ca} \tag{5}$$

where ϵ_{ca} is the axial compression at the backbone.

At the na, $x = d_{na}$. Combining (3), (4), (5), with the definition of na yields:

$$0 = \epsilon_{ca} + \kappa_{na} d_{na} \tag{6}$$

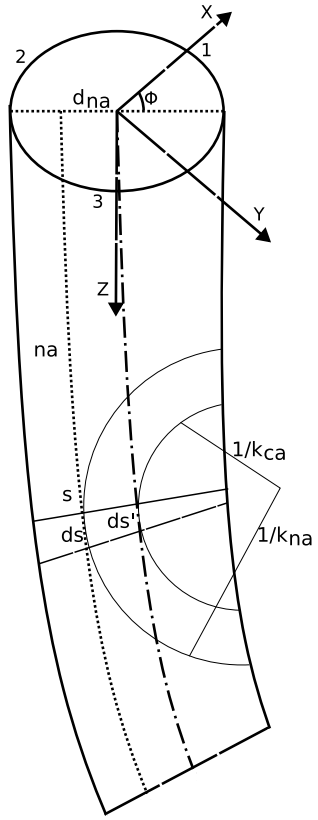

Fig. 1. Section and differential element.

thereby locating the na in the ϕ plane. Switching the origin to na, we obtain:

$$\epsilon_{ca}(s) = \kappa_{na}(s) d_{na} \tag{7}$$

Note that d_{na} cannot be dependent on s because that would violate the assumption of cross-sections remaining planar.

B. Constitutive equations

Using Hooke's law, we relate the compression of the differential element to the tendon tensions:

$$\sum_{i=1}^{3} T_i(s) = K_a \epsilon_a(s) \tag{8}$$

where K_a is the axial compressive stiffness of the backbone and $T_i(s)$ is the tension in the i^{th} tendon at na coordinate s.

Assuming small deflections, no shear deformation, and no torsion, the local bending moment for linear elastic bending, M, is given by:

$$M(s) = K_b \kappa_{na}(s) \tag{9}$$

where K_b denotes the bending stiffness of the section.

As before, superposition of strain allows us to consider moments due to the tendon tensions at the center of the differential element. Using the assumption that cross sections remain planar after deflection, the three tendons are orthogonal to the differential element. Moment $M_i(s)$, at the center due to each of the tendons is given by:

$$M_i = R \times T_i = R T_i sin(\pi/2) \tag{10}$$

where $i \in [1, 3]$ and R is the radius of the section with the tendons located at its circumference.

C. Anisotropic axial compression

In the case of planar bending [24] established:

$$d_{na} = \frac{K_b}{K_a d_{actuator}} \tag{11}$$

where $d_{actuator}$ is the radial distance of the actuating tendon.

For spatial bending, equations (7), (8), (9), (10) need to be solved simultaneously to locate the d_{na} spatially. This was done implicitly in [25]. Our work extends [25] by exploiting the spatial variation of d_{na} with the bending plane, ϕ. As an overview of the rest of this paper - we capture this variation analytically for a special case and subsequently propose the EC approach to compensate for it during control. The dependence of $d_{na}(\phi)$ in ϕ implies that axial compression, as given by (7), changes with the bending plane. This is the key reason why kinematics, which assume constant backbone length, result in varying spatial bending of TDCRs with compressible backbones. The variations manifest as a reduction in curvature and non uniform EE speeds.

We *posit* that this variation of d_{na} with bending plane is identical for all TDCRs with compressible backbones and proceed to analyse the case where a backbone exhibits axial compression significant enough for the na to move to the circumference at certain bending planes, e.g. a rubber backbone or in our case, a steel mesh reinforced rubber hose used in concrete pumping [6].

Constrained beam loading: We now consider mixed mode beam bending, where the beam is loaded by tendon/s under tension and is simultaneously constrained by other locked tendon/s imposing displacement constraints. This can be interpreted as longitudinal 'squeezing' of the section. We assume ideal tendons with no tendon stretch and, initially, we do not allow tendons to unspool beyond initial section length, s. For our special case of a highly compressible backbone, this implies that the ns will pass through the tendon/s held at length s. Considering this special case helps avoid the conversion of displacement constraints into force constraints and ensuing analytical complexity of mixed mode beam bending.

Consider the case when two tendons, 1 and 2, are free to spool up, and the length of the third tendon, 3, is held constant at initial length, s, allowing the section to bend at any $\phi \in [0, 2\pi/3]$ as shown in Fig. 2 .

Using geometry, the distance of the ns from the center is given by:

$$d_{na}(\phi) = Rcos(\pi/3 - \phi) \tag{12}$$

Fig. 2 shows the locus of na as ϕ varies from $[0, 2\pi/3]$. Note that the na must lie at or inside the circumference of cross section when one tendon is held at initial length.

For planar bending, [24] showed that the backbone length is coupled with its curvature. We have shown the coupling between backbone length and the plane of bending for spatial bending of a section with three tendons, and emphasise the use of three shape space degrees of freedom (DOF) for robots with a (even slightly) compressible backbone, bending spatially - ϕ, $\kappa_{ca}(s)$, and $\epsilon_a(s)$. The shape space can be represented by a different set of three DOFs but we chose the ones that are easily measurable/specified and are consistent with prior literature [24], [25]. To control the three shape space DOFs, three actuator space DOFs are required, which are supplied by the three tendons.

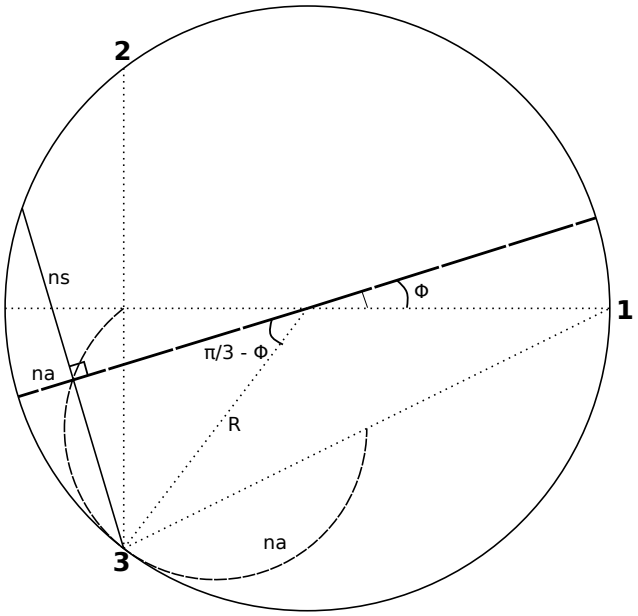

Fig. 2. A cross section showing ns when tendons 1 and 2 retract and tendon 3 is held constant at initial length, s. The locus of the na as ϕ varies between $[0, 2\pi/3]$ is also shown.

D. 3D statics

Next, we decompose the vector moments in two directions resulting in zero moment in the bending plane and resultant moment orthogonal to it:

$$\begin{aligned} M_1 cos(\phi) + M_2 cos\Big(\frac{2\pi}{3} - \phi\Big) + M_3 cos\Big(\frac{4\pi}{3} - \phi\Big) &= K_b \kappa_{na} \\ M_1 sin(\phi) - M_2 sin\Big(\frac{2\pi}{3} - \phi\Big) - M_3 sin\Big(\frac{4\pi}{3} - \phi\Big) &= 0 \end{aligned} \tag{13}$$

Assuming superposition, using (10) in (13) to obtain the equations above in terms of tendon tensions and combining them with (8):

$$\begin{bmatrix} cos(\phi) & cos(\frac{2\pi}{3} - \phi) & cos(\frac{4\pi}{3} - \phi) \\ -sin(\phi) & sin(\frac{2\pi}{3} - \phi) & sin(\frac{4\pi}{3} - \phi) \\ 1 & 1 & 1 \end{bmatrix} \begin{bmatrix} T_1 \\ T_2 \\ T_3 \end{bmatrix} = \begin{bmatrix} \frac{K_b}{R}\kappa_{na} \\ 0 \\ K_a \epsilon_a \end{bmatrix}$$

$$\text{Abbreviating,} \quad A(\phi) \qquad T \quad = \quad K \tag{14}$$

Like (3), in (14), na passes through the centroidal axis due to pure bending. The specification of a configuration of the differential element, $\{\phi, \kappa_{ca}(s), \epsilon_a(s)\}$, fixes the d_{na}. Along with a known R, and measured K_b and K_a (as described

in [24]), the required unique tensions in the tendons can be calculated by,

$$T(s) = A^{-1}(\phi)K(s) \tag{15}$$

Since most TDCRs do not have tension sensing, let alone continuous tension sensing along the length of each tendon, and tendon tensions are needed, at least initially, to determine K_b and K_a, and subsequently for inverse static control, (15) is of limited use. Consequently, the next step in our analysis involves establishing a proportional relation between tendon tension and retraction and determining K without measuring K_b and K_a.

E. Averaged properties

To avoid measurement and specification of $\epsilon_a(s)$ and $T_i(s)$, we define average axial compression, $\bar{\epsilon_a}$ and average tendon tensions, $\bar{T_i}$, quantities that are based only on the specification of backbone curvature, $\kappa_{ca}(s)$. The subscript $_{EE}$ refers to the quantity at the end effector.

Using (7) and (2),

$$\begin{aligned} \epsilon_{ca}(s) &= \frac{\kappa_{ca}(s)d_{na}}{1+\kappa_{ca}(s)d_{na}} \\ \bar{\epsilon_{ca}} &= \frac{1}{s_{EE}}\int_0^{s_{EE}} \epsilon_{ca}(s)ds = \frac{s_{EE}-s'_{EE}}{s_{EE}} \end{aligned} \tag{16}$$

$$\bar{T_i} = \frac{1}{s_{EE}}\int_0^{s_{EE}} T_i(s)ds \tag{17}$$

and using Hooke's law for the averaged axial compression over the section,

$$\sum_{i=1}^{3} \bar{T_i} = K_a\bar{\epsilon_{ca}} \tag{18}$$

EE pitch, θ_{EE}, is given by,

$$\theta_{EE} = \int_0^{s_{EE}} \kappa_{na}(s)ds = \bar{\kappa_{na}}s_{EE} = \bar{\kappa_{ca}}s'_{EE} \tag{19}$$

F. Application to position control

We propose a proportionality between average tendon tension and its retraction from initial length, s_{EE}. We assume that this relation exists for each tendon individually, independent of the length or tension in the other tendons,

$$\begin{aligned} \bar{T_i} &= c(s_{EE} - l_i) \\ &= c\Delta l_i \end{aligned} \tag{20}$$

where l_i is the length of the tendons and c is the constant of proportionality. In the case of highly compressible backbones, negative Δl and therefore, negative tensions do not occur since the na is located at the circumference. Unlike Hooke's law, (20) relates tendon tensions with their length change due to spooling/unspooling, and not directly to the internal tendon strain. The tendons are assumed to be inextensible, e.g. we use nylon sheathed braided steel cables as tendons.

Instead of defining (20) for averaged tensions, we could have defined it for local tensions leading to $l_i(s)$ and then defined an average retraction over the section. However, that would have complicated the analysis herein without altering the results.

Averaging (14) over the section and simplifying using (16), (17) and (19),

$$A(\phi)\bar{T} = \bar{K} = \begin{bmatrix} \frac{K_b}{Rs_{EE}}\theta_{EE} \\ 0 \\ K_a\bar{\epsilon_{ca}} \end{bmatrix} \tag{21}$$

Substituting (20) in (21) and inverting $A(\phi)$,

$$\Delta l = A^{-1}(\phi)\bar{K}/c \tag{22}$$

Recall that d_{na} is a function of ϕ but can be fixed by specifying K. This is also true for $\bar{K}$ because d_{na} cannot change with s. We now have a way to achieve a given shape space configuration with position control of the tendon lengths, for a section with a highly compressible backbone.

G. EC model

This model requires the specification of the EE pitch envelope of the continuum section, defined by its maximum pitch, $\theta_{EE,max}$. The model fixes the axial compression that occurs while bending at the $\theta_{EE,max}$ for all EE pitch values, $\theta_{EE} <= \theta_{EE,max}$, at all bending planes. This guarantees that the backbone length remains constant at every configuration within the section's envelope and the corresponding $\bar{\epsilon_{ca}}$ is the minimum compression required to achieve that backbone length.

In our highly compressible backbone actuated by three tendons example, we know that the maximum compression happens at the midplanes, using (7) and (12). When bending at the midplane, the na is at its furthest location - the circumference. To fix the maximum compression for the spatial envelope, we fix the d_{na} at the circumference as ϕ varies. This is designed to allow tendon spooling/retraction but prohibit tendon unspooling beyond initial length.

It can be seen from Fig. 2 that while bending at the midplane, the retracting tendons have to retract equally, due to symmetry. Therefore, at $\theta_{EE,max}$, at $\phi = 60^o$, tendons 1 and 2 have equal tension and tendon 3 has zero tension and is at initial length. Setting $\bar{K}/c = [1;0;2]^T\Delta l_{i,meas}$ in (22),

$$\Delta l(\phi) = A^{-1}(\phi)\begin{bmatrix} 1 \\ 0 \\ 2 \end{bmatrix}\Delta l_{i,meas} \tag{23}$$

fixes the d_{na} at R as ϕ varies. The scalar $\Delta l_{i,meas}$ is the measured amount of retraction of either of the two retracting tendons for the section to achieve $\theta_{EE,max}$ at a tendon midplane. As $A^{-1}(\phi)$ varies with ϕ, the value 1 fixes the $\theta_{EE,max}$ and the value 2 fixes the axial compression at tendon midplanes at all ϕ.

Preload: While maintaining the entry set to 2 in (23), linear variation of the first element in the interval $[0, 1]$ produces linear variation of θ_{EE} according to (21). When $\theta_{EE} < \theta_{EE,max}$, the na is located outside the section. At a tendon midplane, all three tendons retract to maintain the same backbone compression or length as at $\theta_{EE,max}$ when only two tendons retract. Setting $\theta_{EE} = 0$ straightens the section and all three tendons retract to $0.66 * \Delta l_{i,meas}$, providing us with the minimum tendon preload required to

reach the $\theta_{EE,max}$. This is achieved without initial preload calibration but only requires that the tendons have zero tension at the starting position, i.e.. when the section is in rest position the tendons should hang limply but maintain contact with the end effector.

Maximum workspace volume: A disadvantage of the above approach is that the workspace volume of the section is less than physically achievable because when $\theta_{EE} < \theta_{EE,max}$, the section experiences more compression than physically necessary. In some cases, holding the section at the minimum compression required at $\theta_{EE,max}$ for a long time could potentially damage the backbone, especially when there is little time spent at $\theta_{EE,max}$. In this situation, substituting the vector in (23) with $[i; 0; 2i]^T$ where $i \in [0, 1]$ establishes the minimum axial compression necessary to locate the na at the circumference. This mode of operation lets us achieve maximum workspace volume, minimum required backbone compression at all curvatures but the EE pitch variation is non-linear according to (14). When $i = 0$, the section is straight and does not experience any axial compression assuming the initial section position has tendons under zero tension. Therefore, this mode of operation does not require any tendon preloading.

Application of this algorithm will subject a section that is not highly compressible to very high tendon tensions that could potentially damage the backbone or the tendons. We now introduce a tunable parameter, $\alpha \in [0, 1]$. Axially stiff backbones, e.g. carbon tubes, will have an α near zero while for highly compressible backbones it will approach unity. Using α we fix the d_{na} at its apogee instead of R. Substituting the vector in (23) with $[1; 0; 2\alpha]^T$ or $[i; 0; 2i\alpha]^T$, depending on the mode of operation relaxes the constraint on tendon displacement, allowing the tendons to unspool to lengths dictated by the section's material properties when α is properly tuned. One approach to to tuning the value of α is to move the EE in a circle. Initializing at $\alpha = 0$ sets the backbone compression to zero and EC retrieves the kinematic solution which does not consider axial compression. If the EE slows down near tendon planes or if tendons become visibly slack, the α value can be increased.

Note that it is possible that the third entry in the vector might be required to have value slightly greater than 2 due to the nonlinearities introduced by the use of spacers to route the tendons.

To summarize, the algorithm introduced herein can be used to control the bending plane ϕ and EE pitch θ_{EE} of a continuum section, compensating for axial compression without knowledge or measurement of material properties (K_b, K_a), shape space properties $(\kappa_{ca}(s), \kappa_{na}(s), s', \epsilon_{ca}(s))$, or tendon tensions. The approach can be applied to sections with non-constant curvature, and does not require preloading during calibration. In comparison with the work in [24], our proportionality based approach avoids the use of filtering of input configurations to only allow ones with sufficient ϵ_a. Inverting the A matrix for n-tendons coupled with [1;0;2α] results in guaranteed positive tensions in highly compressible backbones. (We note that tuning would be needed to guarantee positive tensions in relatively incompressible backbones to operate without potentially damaging the section.)

III. Experimental Validation

The EC approach described above was implemented on the combined distal and proximal section of a two section tendon driven continuum hose robot. This robot, designed for 3D printing of cement in construction applications [6], features as its backbone an industrial cement hose. Each of its sections is driven by three tendons spaced radially 120^o apart, routed through spacers on the outside of the hose. The distal secion's tendons are actuated and the proximal section's tendons are let out such that they do not affect bending of the combined section. The tendon lengths are sensed at the actuator level using encoders at the motors. The robot has no tendon tension sensing. Under the tendon loading required to operate the robot, the backbone exhibits significant axial compression as shown in Fig. 3. An IMU (not shown), ICM-20948, has been attached to the EE with its z-axis tangential to the centroidal axis providing logging capability of EE pitch and robot bending plane.

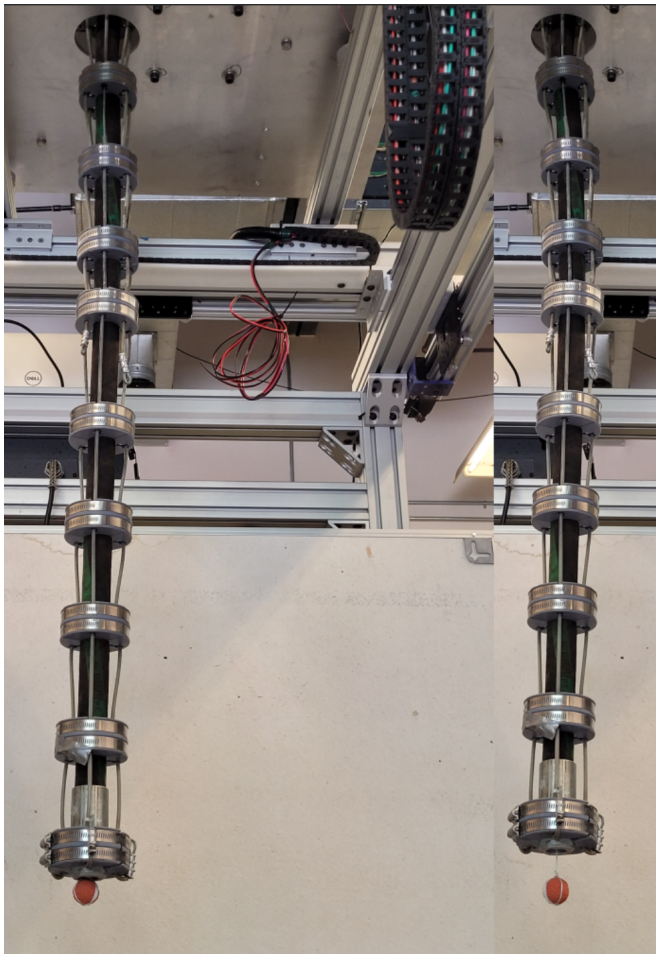

Fig. 3. Extent of axial compression of the continuum hose shown by the protruding string. The picture on the left is at initial configuration with tendons barely under any tension and the picture on the right shows the effect of the vector [0;0;1.8] in (23).

The EC algorithm introduced in this paper was evaluated for a circular trajectory (with constant velocity) of the EE. The performance of the robot was compared to that when implementing, for the same tip trajectory, previously established inverse kinematics.

Figs. 4 and 6 show the tendon length changes measured by the encoders over a time period of 18 seconds for both models. The EC model vector in this comparison is [1;0;2.4] and we, therefore, see that the tendons always remain shorter than the initial length in Fig. 6.

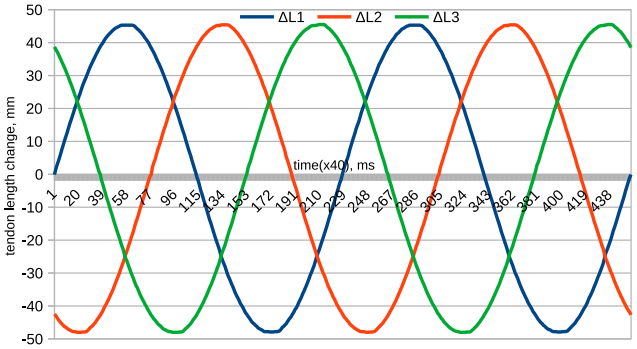

Fig. 4. Tendon length change from initial initial length, s, using inverse kinematics. Positive values denote extension.

Figs. 5 and 7 are scatter plots of the EE pitch θ, with bending plane, ϕ measured by the tip mounted IMU. The distal section's tendons are located at 60^o, 180^o, and 300^o respectively. We note that the EC model significantly outperforms the kinematics model. For the EC model in Fig. 7 , the peak-to-peak variation of EE θ is 9°, compared to kinematic model's θ variation of 27°. We also notice that the EE speed is more uniform for the EC model by observing the relatively uniform density of the scatter points. We see, in Fig. 5, that the EE speeds up in the tendon midplanes and slows down in the plane of the tendons.

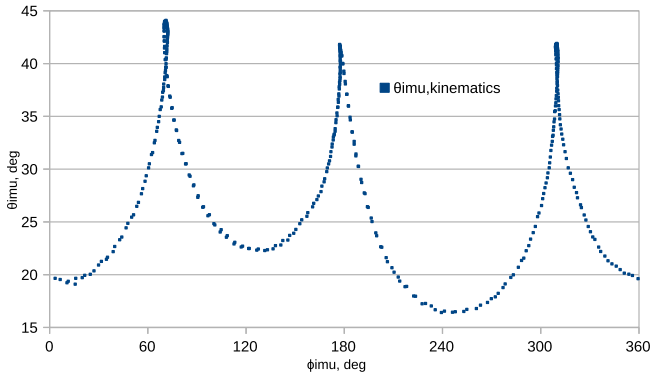

Fig. 5. Spatial variation of end effector pitch, θ, with bending plane, ϕ, under inverse kinematics. We see a variation of 27°, with peaks in the tendon planes and valleys in the midplanes. The variation in the scatter of points indicates faster speed of the EE in the midplanes.

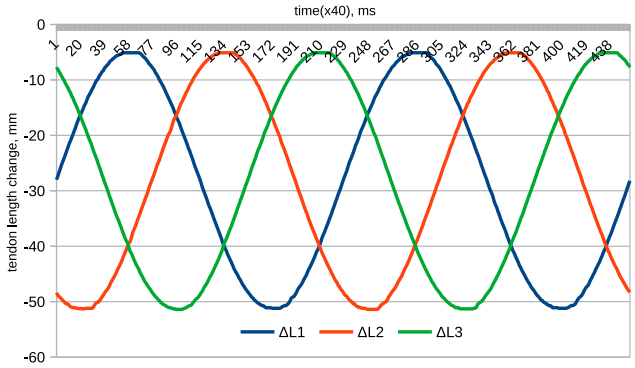

Fig. 6. Tendon length changes from initial length, s, using the EC model. Note that the tendons never extend beyond initial length due to the EC model vector, [1;0;2.4].

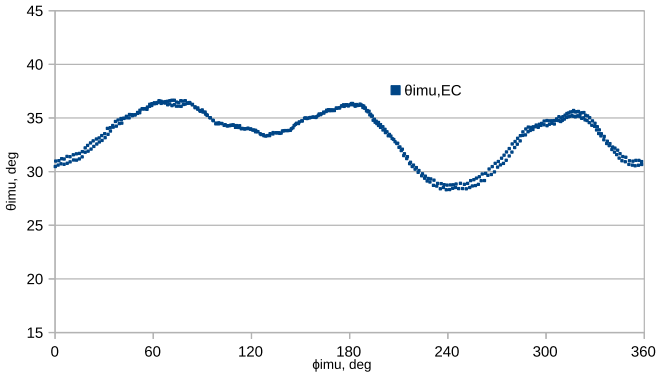

Fig. 7. Spatial variation of the EE pitch, θ, with the bending plane, ϕ using the EC model. We see a peak-to-peak variation of 9°, a significant improvement over the inverse kinematics model. We also note that the EE speed remains uniform over the circular trajectory as indicated by the uniform scatter of points.

IV. Conclusions

We have discussed the effects of unmodeled axial backbone compression in tendon driven continuum robots and the consequent reduction in controller performance. We introduced a new approach, based on active placement of the neutral axis, to compensate for axial compression. The approach does not require tendon tension sensing or estimation of robot materials properties, required in previous approaches. Implementation of the new approach on a tendon driven hose robot exhibiting significant axial backbone compression demonstrates its effectiveness when compared to implementations based purely on kinematics.

References

[1] R. J. Webster and B. A. Jones. Design and kinematic modeling of constant curvature continuum robots: A review. *International Journal of Robotics Research*, 29(13):1661–1683, 2010.

[2] I. D. Walker, H. Choset, and G. Chirikjian. Snake-like and continuum robots. In *Springer Handbook of Robotics*, chapter 20, pages 481–498. Springer, 2nd edition, 2016.

[3] J. Burgner-Kahrs, D. C. Rucker, and H. Choset. Continuum robots for medical applications: A survey. *IEEE Transactions on Robotics*, 31(6):1261–1280, 12 2015.

[4] M. Wang, D. Palmer, X. Dong, D. Alatorre, D. Axinte, and A. Norton. Design and development of a slender dual-structure continuum robot for in-situ aeroengine repair. In *Proceedings IEEE/RSJ International Conference on Intelligent Robots and Systems (IROS)*, pages 5648–5653, 2018.

[5] R. Buckingham. Snake arm robots. *Industrial Robot: An International Journal*, 29(3):242–245, 2002.

[6] M. Srivastava, J. Ammons, A.B. Peerzada, V.N. Krovi, P. Rangaraju, and I.D. Walker. 3d printing of concrete with a continuum robot using variable curvature kinematics. In *Proceedings IEEE International Conference on Robotics and Automation (ICRA)*, pages 3216–3222, 2022.

[7] S. Kamtikar, S. Marri, B.T. Walt, N.K. Uppalapati, G. Krishnan, and G. Chowdhary. Towards autonomous berry harvesting using visual servoing of soft continuum arm. In *Proceedings AI for Agriculture and Food Systems*, pages 1–7, 2021.

[8] M. Wooten, C. Frazelle, I. D. Walker, A. Kapadia, and J. H. Lee. Exploration and inspection with vine-inspired continuum robots. In *Proceedings 2018 IEEE International Conference on Robotics and Automation (ICRA)*, pages 1–5. IEEE, 5 2018.

[9] G. Tan, H. Hidalgo, H-L Kao, I.D. Walker, and K.E. Green. A continuum robot surface of woven, mckibben muscles embedded in and giving shape to rooms. In *Proceedings IEEE International Conference on Robotics and Automation (ICRA)*, pages 11432–11437, 2022.

[10] M.M. Dalvand, S. Nahavandi, and R.D. Howe. An analytical loading model for n-tendon continuum robots. *IEEE Transactions on Robotics*, 34(5):1215–1225, 2018.

[11] T. Kato, I. Okumura, H. Kose, K. Takagi, and N. Hata. Extended kinematic mapping of tendon-driven continuum robot for neuroendoscopy. In *Proceedings IEEE/RSJ International Conference on Intelligent Robots and Systems (IROS)*, pages 1997–2003, 2014.

[12] M. Neumann and J. Burgner-Kahrs. Considerations for follow-the-leader motion of extensible tendon-driven continuum robots. In *Proceedings IEEE International Conference on Robotics and Automation (ICRA)*, pages 917–923, 2016.

[13] W.R. Wockenfuss, V. Brandt, L. Weisheit, and W-G Drossel. Design, modeling, and validation of a tendon-driven soft continuum robot for planar motion based on variable stiffness structures. *IEEE Robotics and Automation Letters*, 2022.

[14] Z. Zhang, J. Dequidt, J. Back, H. Liu, and C. Duriez. Motion control of cable-driven continuum catheter robot through contacts. In *IEEE Robotics and Automation Letters, presented at IEEE International Conference on Robotics and Automation*, 2019.

[15] D. Trivedi, C. D. Rahn, W. M. Kier, and I. D. Walker. Soft robotics: Biological inspiration, state of the art, and future research. *Applied Bionics and Biomechanics*, 5(3):99–117, 12 2008.

[16] B. Jones and I.D. Walker. Kinematics for multi-section continuum robots. *IEEE Transactions on Robotics*, 22(1):43–55, 2006.

[17] J. Lu, F. Du, F. Yang, T. Zhang, Y. Lei, and J. Wang. Kinematic modeling of a class of n-tendon continuum manipulators. *Advanced Robotics*, 34(19):1254–1271, 2020.

[18] N.C. Chairopoulos, P. Vartholomeos, and E. Papadopoulos. Modeling, simulation, and experimental validation for a tendon-driven soft arm robot configuration – a continuum mechanics method. In *Proceedings IEEE/RSJ International Conference on Intelligent Robots and Systems (IROS)*, pages 5695–5700, 2019.

[19] P. Gonthina, M.B. Wooten, I.S. Godage, and I.D. Walker. Mechanics for tendon actuated multisection continuum arms. In *Proceedings IEEE International Conference on Robotics and Automation (ICRA)*, pages 3896–3902, 2020.

[20] S. Hirose. *Biologically Inspired Robots*. Oxford University Press, 1993.

[21] F. Renda and C. Laschi. A general mechanical model for tendon-driven continuum manipulators. In *Proceedings IEEE International Conference on Robotics and Automation (ICRA)*, pages 3813–3818, 2012.

[22] J.A. Schultz, H. Sanders, P.D.H. Bui, and M. Killpack. Modeling the dynamics of soft robots by disks and threads. In *Proceedings IEEE International Conference on Robotics and Automation (ICRA)*, pages 3223–3229, 2022.

[23] K. Oliver-Butler, J. Till, and D.C. Rucker. Continuum robot stiffness under external loads and prescribed tendon displacements. *IEEE Transactions on Robotics*, 35(2):403–419, 2019.

[24] D.B. Camarillo, C.F. Milne, C.R. Carlson, M.R. Zinn, and J.K. Salisbury. Mechanics modeling of tendon-driven continuum manipulators. *IEEE Transactions on Robotics*, 24(6):1262–1273, 2008.

[25] D.B. Camarillo, C.R. Carlson, and J.K. Salisbury. Configuration tracking for continuum manipulators with coupled tendon drive. *IEEE Transactions on Robotics*, 25(4):798–808, 2009.

[26] A. Bajo and N. Simaan. Finding lost wrenches: Using continuum robots for contact detection and estimation of contact location. In *Proceedings IEEE International Conference on Robotics and Automation (ICRA)*, pages 3666–3673. IEEE, 5 2010.

[27] M.B. Wooten and I.D. Walker. Environmental interaction with continuum robots exploiting impact. *IEEE Robotics and Automation Letters*, 7(4):10136–10143, 2022.